

Air Flow Structure Over Short-gravity Breaking Water Waves

Nicolas Reul, Hubert Branger, Jean-Paul Giovanangeli

Abstract Despite its importance for momentum and mass transfer across the air–sea interface, the dynamics of airflow over breaking waves is largely unknown. To fill this gap, velocity and vorticity distributions above short-gravity breaking waves have been measured in a wind-wave tank. A Digital Particle Image velocimetry technique (DPIV) was developed to accomplish these measurements above single breaking waves, propagating in mechanically-generated wave groups and forced by the wind. By varying the wind speed and initial characteristics of the groups, the airflow structure was captured over waves at different stages of the breaking process, and breaking with various intensities. The instantaneous airflow that separates from a sharp breaking crest is very similar to that occurring over a backward facing step. The separation bubble is however strongly unsteady: the steeper the wave crest and the larger the Reynolds number based on the crest-height, the higher the separated layer and the farther downwind the reattachment point. Instantaneous flow topology displays specific features of three-dimensional separation patterns. The tangential stress above the wave profile does not exhibit spikes at reattachment but grows progressively downwind from zero at reattachment to a value at the next crest approximately that found at the upwind breaking crest. Static pressure measurements revealed that large pressure falls are generated by vortices in the separated layer, as found in separated flows over solids. This study may provide useful data for theoretical and numerical modelling of the flow and associated phenomena.

Keywords Breaking wind waves · Separation of the air flow · Sea drag

N. Reul (✉)

Laboratoire d’Océanographie Spatiale, Institut Français de Recherche et d’Exploitation de la Mer (IFREMER), 29200 Plouzané, France

e-mail: nreul@ifremer.fr

H. Branger · J.-P. Giovanangeli

Laboratoire IOA, Institut de Recherche Sur les Phénomènes Hors Equilibre (IRPHE), Case 903, 163, avenue de Luminy, 13288 Marseille, France

1 Introduction

Because of their particular dynamics, breaking waves form specific and severe *transient hydrodynamic disturbances* at the sea surface. The breaking phenomenon is thus nonlinear since it concerns waves with large steepnesses, ak , of order one, where a is the wave amplitude and k the wavenumber. As consequences of breaking, highly rotational and turbulent two-phase flows are locally generated under and at the interface near the breaking crests and they interact with the underlying wave motions. Whether plunging, spilling or micro-breaking, breakers therefore exhibit surfaces in the region of the crests with discontinuous kinematic conditions (occurrence of stagnation points) and sharp local geometry. Moreover, in deep water, wave breaking is an essentially intermittent process, both in time and space. This is due to the fact that high waves occur in groups, and since the phase velocity exceeds the group velocity, individual waves tend to move forwards relative to the group. They then break only for a limited time during which their steepness exceeds a certain threshold within the groups.

In this paper, we shall consider aspects of such breaking sea state from an aerodynamical point of view. It was indeed shown experimentally by Banner and Melville (1976) that the occurrence of whitecaps or patches of rough water near the crests of steep gravity waves tended to induce separation of the airflow over the wave. Simpson (1989) defines boundary-layer flow separation as the *complete process of departure, detachment or breakdown of the boundary-layer flow. The detachment is accompanied by a sudden thickening of the rotational flow near the wall and by large values of the normal component of the velocity at the wall*. For these reasons, breaking waves also induce specific and severe *transient aerodynamic disturbances* just over the sea surface. Here, we investigate this particular geophysical aspect in an experimental manner. Breaking waves are simulated in the laboratory and we try to characterize the detailed turbulent structure of the separated airflow past such unsteady water obstacles.

Understanding of the airflow dynamics over breakers is essential for the parameterization of momentum and mass transfer processes across the air-sea interface. Airflow separation (AFS) over breaking waves indeed modifies the local nature of the wind stress. On the one hand, laboratory measurements conducted in moderate wind forcing conditions of the pressure and horizontal velocity in the air stream over standing breaking waves by Banner and Melville (1976) and Banner (1990) thus indicate that the flux of horizontal momentum from the air to the water is increased locally by a factor of order 50, due to airflow separation. Therefore, the AFS mechanism over short breaking waves may play an important role in the growth of wind waves. On the other hand, airflow separation above breaking waves was recently invoked by Donelan et al. (2004), and Kudryavtsev and Makin (2007), as a potential mechanism responsible for the reported saturation of the drag coefficient at very high winds. At very high winds and in conditions of continuous breaking, the flow may indeed separate from breaking crest to breaking crest (reattachment near the crest of each preceding wave). In these cases, the outer flow is unable to follow the wave surface, does not “see” the troughs of the waves and the tangential stress almost completely vanishes. The fact that breaking crest density saturates at very high winds (whitecap coverage tends towards 100%), together with the impact of AFS, may explain that the aerodynamic roughness approaches a limiting value in high winds. The possibility of a limiting state in the aerodynamic roughness of the sea surface through the AFS mechanism is of critical importance in understanding and modelling the development of hurricanes and other intense storms. How to incorporate these two effects of AFS in the parameterizations of the wind energy input to wave fields is however a very difficult and challenging task. Recent modelling attempts by Kudryavtsev and Makin (2001)

allow explicit assessment of the impact of air-flow separation from wave breaking crests on the sea-surface drag assuming the dynamics of the separated air flow over breaking waves is similar to that over the backward facing step.

Nevertheless, one of the unresolved issues is the effect of breaking wave unsteadiness on the wind stress. As argued by Longuet-Higgins and Smith (1986), since breaking is essentially intermittent by nature, the separation of the airflow is therefore likely to be intermittent also. This may cause the horizontal stress exerted by the wind to be locally both intermittent and patchy. For the moment, very little is known about these wind stress intermittencies. Little is also known about the contributions of normal and tangential components of the wind stress to total stress in the presence of breaking waves. Banner and Peirson (1998) have however recently shown that the tangential-stress-averaged contribution stays approximately constant whether the water surface is smooth or covered by steep and micro-breaking waves. Consequently, even in the presence of numerous short breaking waves, the surface cannot be considered as fully aerodynamically rough. Moreover, as the waves grow and begin to break, the total stress may increase by a factor of 5 (Belcher 1998); a process is therefore responsible for the large enhancement of the normal wind stress contribution to the total stress: airflow separation over short breakers is a very likely candidate. However, the static pressure evolution at the surface during a complete breaking event, which is key information for understanding airflow separation effects on the momentum transfer from air to water, is not known at the moment. Therefore, it is still not certain whether breaking wave effects on the airflow play an important role on the energy balance in wind-wave fields. It was thus suggested by Belcher (1998), that these effects may be responsible for the discrepancies between observation and theory concerning the wave-growth-rate dependence with wave age, especially for young waves (waves such that $c/u_* \leq 5$, where c is the phase speed and u_* , the wind friction velocity).

Dynamics of the airflow over breakers also play a crucial role in sea-spray droplets entrainment and production mechanisms. As soon as the wind-speed exceeds 7 m s^{-1} , laboratory (Koga and Toba 1981), as well as field (DeLeeuw 1986) measurements indicate double-maxima in the vertical profiles of sea-spray droplet concentration over the waves. Using a very simple model, DeLeeuw (1987) suggested that the rotor-like structure generated by airflow separation over breakers may be responsible for these double-maxima distributions observed near the wavy surface. Inertial and gravitational effects would keep giant particles recirculating at the borders of the rotor-like air motions downwind of the crests and this would generate two distinct peaks of sea-spray concentration over the water surface. More data are needed to verify this hypothesis. Recent models of sea-spray entrainment and production (Mestayer et al. 1996; Makin 1998; Kudryavtsev 2006) include models of airflow over the waves but do not incorporate the flow separation over breaking waves because there is no realistic model of the processes involved.

Most models of airflow over waves are indeed restricted to the flow over linear or weakly non-linear waves without discontinuous boundary conditions at the interface. Meaningful modelling of the airflow over breaking waves and interpretation of its effects on the momentum and mass transfer require detailed knowledge of the velocity and turbulence structure within the separated flows. The early literature on the subject (Wu 1969; Chang et al 1971; Barnett and Kenyon 1975; Banner and Melville 1976; Gent and Taylor 1977) is mostly focused on the criterion of appearance of the separation process over the waves. Banner and Melville (1976) were the first to establish that airflow separation occurs only if a stagnation point exists at the air/water interface and this kinematic condition corresponds to incipient breaking. Though separation may also occur when the waves are not breaking (Weissmann 1986), it seems likely that breaking waves induce separation far more strongly and consis-

tently. Detailed information on the structure of the flow were first given by Kawai (1981, 1982) who clearly visualized airflow separation patterns over short wind-waves. Small-scale vortices and a high shear layer in the air stream were regularly detected in the lee of wind-wave crests. Kawai (1981, 1982) also noticed a large variability in the separated flow structure and often observed a specific flow pattern described as “the blowing up of a low-speed air mass in the lee of some wave crests”; this pattern was interpreted as a signature of the end of the separation process. However, the important reattachment point was not clearly identified, and his experiments also revealed that airflow separation only occurs over waves that exhibit a maximum value of the local slope along the profile near the crest, greater than 0.6. Kawamura and Toba (1988) later performed velocity–shear measurements in the airflow at a fixed level over short wind-waves. They detected shear spikes over the waves that were attributed to the crossing of instruments through the separated layers. They then deduced an averaged location of the separated shear-layer over the waves and interpolated the averaged reattachment point at the surface. In both the Kawai (1981, 1982), and Kawamura and Toba (1988) experiments, the flow was only investigated over the so-called *micro-breaking waves* while typical wind waves are often breaking more intensively. Moreover, the region of the flow extending from the free surface to the separated shear layer, the unsteadiness of the reattachment length and the dynamics of the separated layer during breaking were not resolved. Also, the nature of the dimension of the flow within the separated regions and at reattachment is still unknown.

Precise measurements of the velocity field in the close vicinity of a moving water surface that breaks up are indeed very difficult because of the unsteady and nonlinear character of breaking waves. However, Reul et al. (1999) have briefly shown that the use of the digital particle image velocimetry (DPIV) technique provides important insights on the detailed instantaneous structure of the flow over unsteady breakers. The complete experiments that were conducted in a wind-wave tank and associated results are now presented in detail. In the first part of the paper, we discuss the DPIV technique and methods that were used to measure the velocity and vorticity fields in the air over single breaking waves, propagating in mechanically-generated wave groups and breaking with intensities ranging from gentle spilling to violent plunging. The general structure of the separated flow over breakers is then briefly discussed through typical examples. Qualitative effects of breaking intermittencies on the structure of the airflow are then investigated by capturing the flow over very similar breaking waves but at different stages of the breaking process. Effects of the wind forcing intensity and the geometry of breaking crests on the airflow patterns are then studied and quantitative links between the separation bubble extent, wave-crest steepness and Reynolds number based on the crest height are established. Some aspects concerning the dimension of the flow in the separation bubbles are also presented based on topological analysis of instantaneous streamline patterns. Finally, details on the along-wind distribution of the tangential and normal stresses above the water surface during a breaking event are given.

2 Experimental Equipment and Procedure

The experiments were conducted in the small IRPHE-Luminy wind-wave facility, which is described by Coantic and Favre (1974). The water section is 8 m long, 0.6 m wide, 0.3 m deep and the air-column height is 0.3 m. The overall approach of the present experiment was to produce wave breaking at approximately 4.5 m from the tank entrance; breaking was induced by the coalescence of frequency-modulated single wave packets that were mechanically generated at the upwind end of the tank and forced by the wind action during their propagation along the tank. A DPIV system was then operated at 4.5 m to measure the airflow velocity

field above the water surface during the passage of the highest and breaking wave within the packets.

2.1 Breaking Waves Generation

A vertically-oscillating wedge wavemaker ($0.60 \times 0.16 \times 0.09 \text{ m}^3$) located at the upwind end of the tank was used to generate the coalescing wave packets. As shown by Pierson et al. (1992), the wave energy within mechanically-generated reversed Gaussian wave groups may be focused at a predetermined longitudinal position in a tank x_b , which can be easily predicted by the linear theory of dispersive waves in deep water. If the initial signal amplitude is sufficient, the amplification of wave energy at coalescence induces very local nonlinearities within the group and generation of a single breaking wave. Thus, we chose the reversed Gaussian wave group as our initial conditions at the wavemaker, with input signals given by:

$$\eta(t) = A \exp[f(t, x_b, T, B)] \sin[g(t, x_b, T, B)] \quad (1)$$

where A is the packet envelope amplitude, B and T are characteristic time scales of the modulation within the group, x_b is the coalescence point, and f and g are functions analytically expressed in Drennan and Donelan (1996). Without wind blowing, wave groups generated using (1) were completely determined initially by their amplitude A , their central frequency f_o , their frequency bandwidth Δf , and their focal point position x_b . To decrease the number of parameters of control in the experiments, we respectively fixed the central frequency and frequency bandwidth of the generated groups to $f_o = 1.9 \text{ Hz}$ and $\Delta f = 1.2 \text{ Hz}$ ($B = 6 \text{ s}^{-1}$ and $T = 1.5 \text{ s}$), which yields a non-dimensional spectral parameter for the modulated input wave packets of $\Delta f/f_o = 0.64$. In the presence of wind, during their propagation from the wavemaker to the theoretical focal point x_b , waves within the group were however both amplified due to momentum transfer from the wind and subjected to Doppler effects due to the wind-induced current action. The combined effect of these two processes had a wind-speed dependent strength, but, due to the short duration of the wind action in the present experiments, it mainly induced a downwind shift of the coalescing groups' focal point: the stronger the wind, the farther downwind the actual focal point (Touboul et al. 2006). For wind speeds up to 8 m s^{-1} and the given initial packet amplitude A , empirical adjustment of the value of x_b in Eq. 1 thus enabled generation of propagating waves forced by the wind that were breaking at accurate predetermined time ($\pm 10 \text{ ms}$), and location within the tank ($4.5 \pm 0.03 \text{ m}$). Three capacitance-wire wave gauges located at fetchs of 1.2, 4.45 and 4.55 m were temporarily used to measure the groups characteristics during their propagation. The propagation of a typical wave group forced by a 5.3 m s^{-1} wind is illustrated in Fig. 1.

One can notice the doubling of the group envelope amplitude between 1.2 and 4.45 m due to wave energy focusing and its small decrease between 4.45 and 4.55 m that is a signature of breaking. We respectively used $a_o k_o$ and Epl_o as non-dimensional parameters to characterize the wave packet steepness and potential energy at initial position 1.2 m; a_o being the group envelope amplitude, k_o the central wavenumber within the group, obtained from the measured central frequency f_o using the linear dispersion relationship. Epl_o was given by Griffin et al. (1996):

$$Epl_o = \frac{2k_o^2 \overline{Ep_o}}{\rho g} = \frac{k_o^2}{\tau} \int_0^\tau \eta^2 dt \quad (2)$$

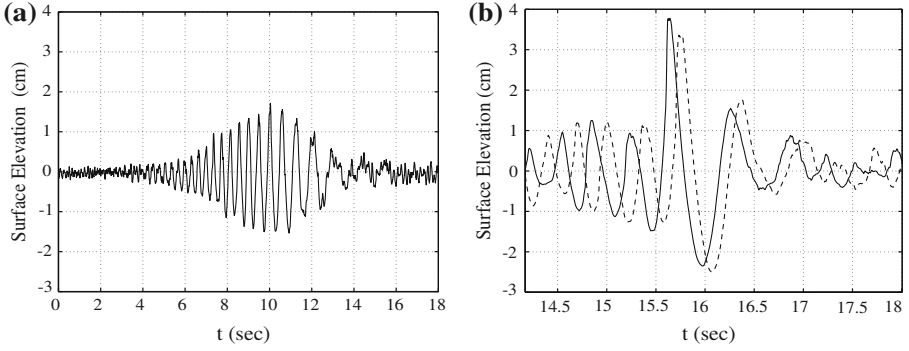


Fig. 1 Propagation of a typical reversed Gaussian wave packet coalescing at $x_b = 4.5$ m and forced by a wind blowing at $U_o = 5.3 \text{ m s}^{-1}$. Surface elevation signals measured at $x = 1.2$ m (a), and (b), at $x = 4.45$ m (solid line) and $x = 4.55$ m (dashed line)

Table 1 Initial group parameters measured at $x = 1.2$ m for the five experimental conditions of input potential energy

f_o (Hz)	Δf (Hz)	$\Delta f/f_o$	$\overline{\eta^2}$ (cm^2)	$a_o k_o$	Epl_o
2.07	1.28	0.617	0.048	0.114	0.0021
2.07	1.28	0.618	0.083	0.161	0.0042
1.83	1.26	0.688	0.134	0.163	0.0055
1.89	1.28	0.679	0.210	0.199	0.0075
1.89	1.16	0.613	0.285	0.226	0.0104

$\overline{\eta^2}$ is the variance of the elevation within the groups

where $\overline{Ep_o}$ is an averaged potential energy within the group per unit time and τ , a time of observation during which the group envelope evolves slowly. Breaking waves with intensities ranging from gentle spilling to violent plunging were thus generated by varying the initial potential energy input into the wave packets. The five initial potential energy conditions that were used throughout the experiments are summarized together with corresponding wave group parameters in Table 1.

2.2 Incident Air-flow Characteristics

During the experiments, we investigated the effects of the wind speed by successively setting the averaged values in the free stream to $U_o = 3.5, 5.3, 6.9, 7.9$ and 10.0 m s^{-1} . The corresponding vertical mean velocity profiles measured at 4.5 m using a Pitot tube are given in Fig. 2.

The lower parts of these profiles exhibit a logarithmic law behaviour from which the wind friction velocity u_* , the height of the boundary layer δ (defined as the location away from the mean water level where $U(\delta) = 0.99U_o$) and the roughness length z_o were deduced in each condition and are given in Table 2.

Note that the wedge-wavemaker was completely immersed in the water at the end of each wave group generation, so that, whatever the wind speed, the wavemaker vertical motion was stopped well before the breaking wave reached the measurement fetch.

Fig. 2 The vertical mean velocity profiles at 4.5 m corresponding to each of the following experimental condition: (\square) $U_o = 3.5 \text{ m s}^{-1}$, (\times) $U_o = 5.3 \text{ m s}^{-1}$, ($*$) $U_o = 6.9 \text{ m s}^{-1}$, (\circ) $U_o = 7.9 \text{ m s}^{-1}$ and (∇) $U_o = 10 \text{ m s}^{-1}$, where U_o is the average wind speed in the free stream

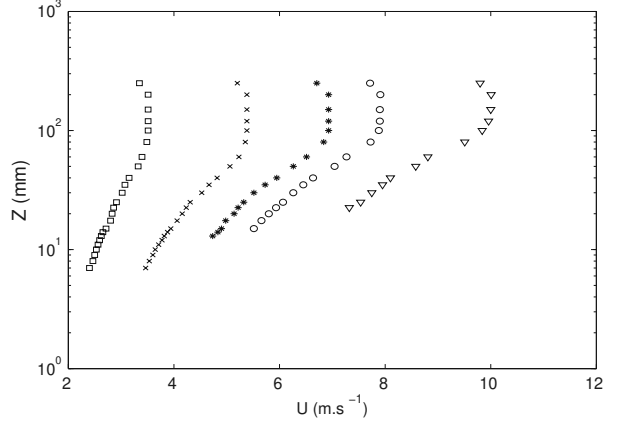


Table 2 Wind friction velocities u_* , boundary-layer thickness δ and roughness length z_o at 4.5 m as a function of the wind speed in the free stream U_o

$U_o \text{ (m s}^{-1}\text{)}$	$u_* \text{ (m s}^{-1}\text{)}$	$\delta \text{ (mm)}$	$z_o \text{ (mm)}$
3.51	0.1442	76	0.0065
5.38	0.259	78	0.0271
6.93	0.347	85	0.0419
7.90	0.395	93	0.0427
10.00	0.506	110	0.0508

2.3 The DPIV Technique

There are four essential system components to any PIV application: suitable fluid tracers, illumination system, particle imaging, and an analysis technique for the acquired images. In the present application, the free-surface treatment of the acquired images was also crucial to determine the velocity and vorticity in the close vicinity of the interface.

The particles used to follow the flow were small water droplets injected by a spray gun at the inlet of the flume. This spray gun features three main controls: size, density and ejection velocity of the water droplets. A 1 mm-aperture nozzle located at the end of a 0.15 m-long copper tube (with diameter 5 mm) was adapted to the gun and used to continuously supply particles into the flow through a small hole in the flume side-wall. The outcoming water droplets were contained in an approximately plane and vertical jet. Tests were conducted to verify that the injection did not generate a significant wake into the flow at 4.5 m. Vertical profiles of the mean wind speed obtained using the Pitot tube were thus compared to mean velocity profiles obtained from the DPIV technique. More than 100 individual PIV measurements were thus performed with the water droplets jet continuously directed against the air stream at the injection point. Averaged velocity profiles obtained from the ensemble of PIV images and Pitot tube only differed by less than about 2%. Optimal droplet size and density were also determined during these preliminary tests. A laser-granulometer system was then used to measure the statistical distribution of particle diameters at a distance of 0.15 m from the spray-gun nozzle. The measurements revealed that more than 90% of the droplets diameters were smaller than $14.9 \mu\text{m}$ with an average value of $7.8 \mu\text{m}$.

We quantified inertial effects for such water droplets in the airflow by considering the motion of particles with density ρ_p evolving in a fluid with density ρ_f , such that $\rho_p \gg \rho_f$. Merzkirch (1974) have shown that, in such conditions, the particle motion is mainly induced by the fluid viscosity, so that the general Basset–Boussinesq–Tchen equation of motion for small, spherical particles can be reduced to:

$$\frac{dU_p}{dt} = \frac{18\mu_f(U_f - U_p)}{\rho_p d_p^2} \quad (3)$$

where U_p , ρ_p and d_p are respectively the velocity, the density and the diameter of the particles, while μ_f and U_f are respectively the dynamical viscosity and the velocity of the fluid. The coefficient $\tau = \rho_p d_p^2 / 18\mu_f$ represents the duration needed for a particle to respond to a step change in the fluid velocity. If we assume that during τ , U_f is constant and that $U_p = 0$ at $t = 0$, the solution of Eq. 3 becomes:

$$U_p = U_f(1 - e^{-t/\tau}). \quad (4)$$

In these experiments, the droplets maximum diameter was $d_{p\max} \simeq 15\mu\text{m}$, so that, with $\rho_{\text{water}} \simeq 998.2\text{ kg m}^{-3}$ and $\mu_{\text{air}} \simeq 1.8 \times 10^{-5}\text{ kg m}^{-1}\text{ s}^{-1}$, the maximum particle relaxation time was about $\tau \simeq 0.7\text{ ms}$. If it is assumed that these droplets follow velocity fluctuations up to a limiting frequency, $n_{\text{Lim}} = 1/2\tau$, a spherical water droplet with diameter $d_p = 15\mu\text{m}$ will follow airflow velocity fluctuations up to approximately 700 Hz.

Gravitational effects for these water droplets in the air were estimated by calculating the terminal velocity of fall of particles suspended in a fluid at rest, which is given by Durst et al. (1981):

$$V_{\text{fall}} = \frac{d_p^2 g}{18\mu_f}(\rho_p - \rho_f) \quad (5)$$

and yields a maximum terminal velocity of fall for the presently used water droplets of about 7 mm s^{-1} . By way of comparison, the zinc particles used by Kawai (1982) had a maximum diameter of $50\mu\text{m}$ and a terminal velocity of fall estimated to be 0.09 m s^{-1} . The effect of gravity on the water particle motions is estimated to generate relative errors less than 1% in almost every area that we investigated in the airflow above the waves.

Arrangement of the PIV imaging and illumination systems is shown in Fig. 3, which contains a side view and a lateral cross-section of the wind-wave tunnel at 4.5 m fetch. As the source of light, we used a twin 12 mJ pulsed Nd:Yag laser located on the tank roof and generating a light beam at 532 nm. The light beam was turned into a light sheet about 1.5 mm thick through a divergent cylindrical lens with focal length 6.4 mm. This light sheet was then directed from above the tank towards the water surface by means of a 45° inclined mirror. To allow complete filming of the upper side of the water surface, the light plane was also slightly inclined at 10° from the upwind/downwind vertical plane. It intersected with the water surface creating a well-defined line, parallel to the wind direction, and located at 0.15 m from the tank side windows. A Charged Coupled Device (CCD) camera with pixel dimensions of $8.9 \times 6.6\mu\text{m}$ and effective resolution of 768 (horizontal) \times 484 (vertical) pixels recorded images of the illuminated particles above the waves, viewing them from the side and looking down with an angle of 10° from the horizontal. The camera was fitted with an appropriate adaptor to couple it with a Micro-Nikkor zoom lens (focal length of 60 mm and f-stop number of 2.8).

Two different field-of-view sizes were used during the experiments and are hereafter denoted *S1* and *S2*. Images of a plastic sheet with a 5 mm-square grid pattern inclined at 10°

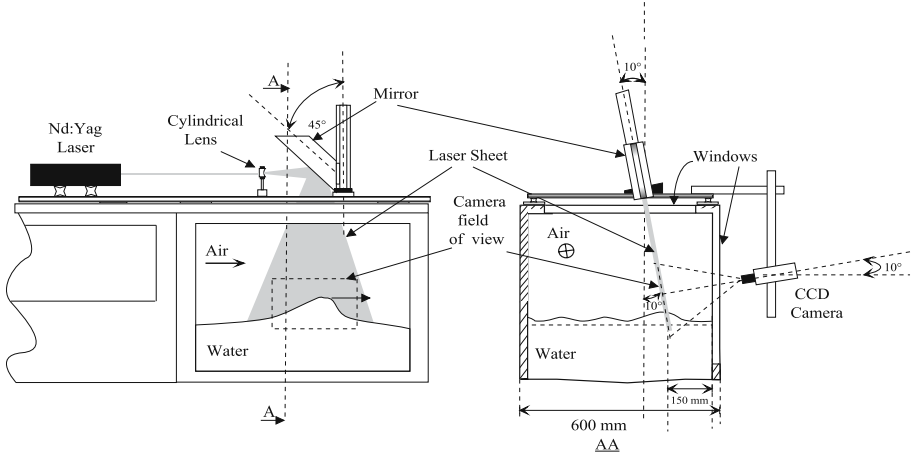


Fig. 3 Arrangement of the PIV system components at the measurement fetch (left: side view; right: lateral cross-section)

from the vertical were used to measure these two sizes. The dimensions of the visualized area were as follows: $0.126 \text{ (horizontal)} \times 0.093 \text{ (vertical)} \text{ m}^2$ for *S1* and $0.257 \times 0.189 \text{ m}^2$ for *S2*. The picture of the still water surface was also used to detect the mean water level.

A cross-correlation DPIV technique similar to that described by Willert and Gharib (1991) was applied. The laser pulse separation between image pairs Δt was set to $100 \mu\text{s}$ and the duration of each pulse δt was $0.01 \mu\text{s}$. Cross-correlation was processed with interrogation window size of $32 \times 32 \text{ pixels}^2$ with 50% overlap. A Gaussian window was applied to each interrogation area before the FFT processing that was performed to calculate correlations. In order to detect the correlation peaks with a subpixel accuracy, after the FFT processing, a two-dimensional symmetrical Gaussian curve fit was performed over three points to interpolate widths, heights and positions of the peaks. A two-dimensional band-pass filter operating on the correlation plane prior to peak detection and subpixel interpolation was also used to remove background noise. The data processing resulted in a field measurement of 49×29 velocity vectors and in a spatial wavelength resolution which was $2.6 \times 3.4 \text{ mm}^2$ for *S1* and $5.3 \times 6.2 \text{ mm}^2$ for *S2*. To enhance the contrast between air and water, the latter was coloured by fluoresceine.

As illustrated in Fig. 4, upper part of images is composed of illuminated particles superimposed on a black background, but the lower part of images is filled by the water image. For each PIV image acquired, it was imperative to treat the image area under the free surface/laser-sheet intersection to accurately determine the actual particle displacements in the interrogation area spanning air and water. First, the free-surface profile was thus detected in each image within pairs. Second, the area under and including the free surface was masked by affecting a constant, dark, grey-level value to each pixel within these areas. Since the area under the free surface had no particles, the cross-correlation produced a zero shift. Interrogation windows that incorporated part of the image below the free surface and above the free surface therefore produced cross-correlation peaks that were due only to particle shifts over the free surface. For these windows, results were only considered valid when the window's centre was either at or above the free surface. The free-surface profile detection was automatically achieved through an image segmentation algorithm based on the grey-level distribution properties within images. Owing to the high contrast between air and water, the

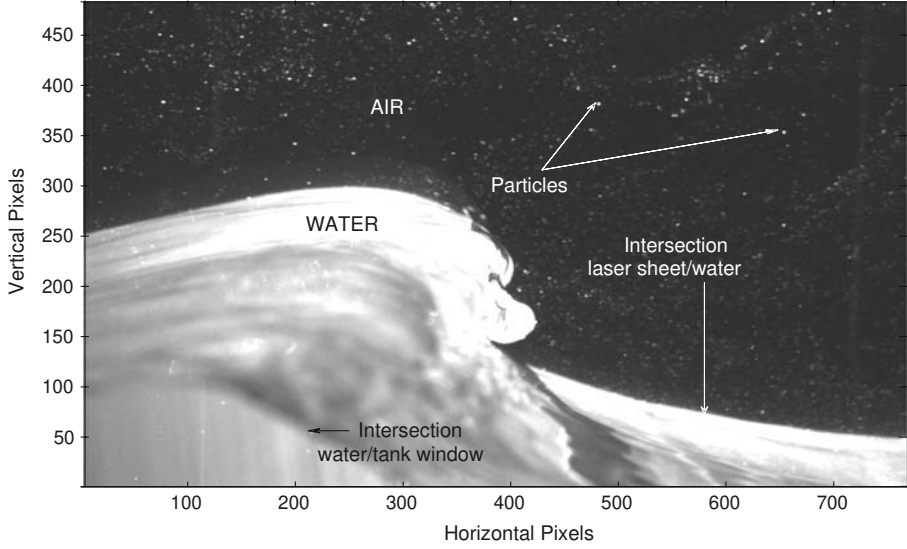


Fig. 4 Example of particles image directly acquired above a breaking wave

distribution of intensities within images was globally bimodal, as shown in Fig. 5a. Image histograms $h(a)$ were thus exhibiting a first high and narrow peak at about grey-level value $a_1 \simeq 10$ (mode 1), and a second lower and wider peak at around $a \simeq 50$ (mode 2). The first mode is due to the dark background in the air-side image while the second mode is associated with light diffusion from both particles and the water surface. Since the free-surface image is the main physical border between these differently contrasted areas within images, it can be determined from the knowledge of a threshold grey-level value a_{lim} , dissociating the two modes. The latter was determined by the first zero up-crossing passage of $\partial h(a)/\partial a$ in the grey-level range $[a_1, 256]$. A contour detection algorithm was then applied to images at that level (see Fig. 5b). The longest isoline detected at level a_{lim} in the images was found to be a good approximation of the free surface. The water profile position was thus determined in approximately 90% of the treated cases with an accuracy of ± 1 pixel (± 0.2 mm for $S1$ and ± 0.5 mm for $S2$). However, specular reflections towards the camera and particle aggregates located close to the free surface sometimes produced spurious patches of light in the images. A visual check-up was therefore necessary to eliminate image pairs with such special features.

In almost any PIV measurement, incorrect vectors are produced due to noise peaks in the correlation function. It is necessary to detect these few vectors using validation methods and to substitute them. The validation was done in two steps. At first, following Keane and Adrian (1992), the highest and the second highest peaks were detected in the correlation plane and vectors for which the ratio between these two respective peak values was smaller than 1.2 were rejected. Second, vectors with very high norm compared to their neighbours were rejected. Rejected vectors then produced discontinuous grid data which were inconvenient when computing vorticity and streamlines. They were therefore substituted using an interpolation scheme known as “Adaptative Gaussian Windowing” (AGW), described by Agui and Jimenez (1987) and also applied to PIV data by Spedding and Rignot (1993).

Spatial velocity gradients were computed using a spline interpolation technique (Spedding and Rignot 1993). A least-squares estimation of coefficients a_j , b_j , c_j and

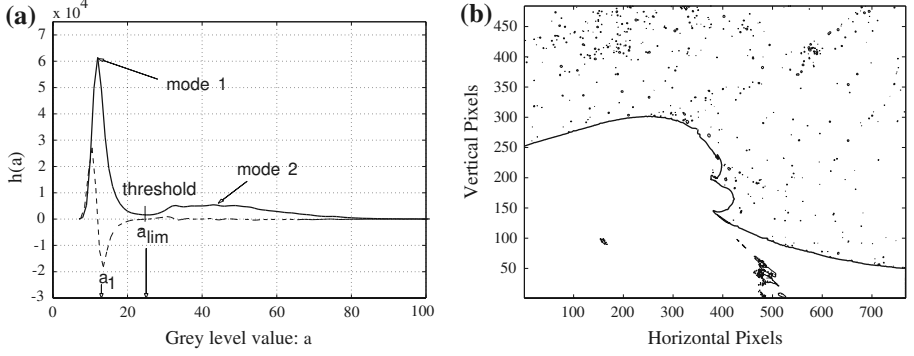


Fig. 5 (a) Smoothed grey-level histogram $h(a)$ computed from the image in Fig. 4 (thick line) and corresponding derivative function $\partial h(a)/\partial a$ (dashed line). (b) Contour plots of the image in Fig. 4 at grey-level a_{lim} ; the thick line is the longest isoline

$\lambda_j(i)$ ($i = 1, \dots, N$) for a two-dimensional spline thin-shell function (STS) was conducted locally from the velocity component $v_j(M)$ at point M :

$$v_j(M) = a_j + b_j X + c_j Z + \sum_{i=1}^N \lambda_j(i) MM_i^2 \ln(MM_i)^2 \quad (6)$$

where $j = (X, Z)$, X being the alongwind direction and Z the vertical. The first advantage of this technique is that it then gives analytical formulae for reconstruction of the spatial velocity gradients:

$$\frac{\partial v_j(M)}{\partial X} = b_j + \sum_{i=1}^N 2\lambda_j(i) MM_i (\ln MM_i^2 + 1), \quad (7a)$$

$$\frac{\partial v_j(M)}{\partial Z} = c_j + \sum_{i=1}^N 2\lambda_j(i) MM_i (\ln MM_i^2 + 1). \quad (7b)$$

Moreover, interpolation points need not be given in a rectangular domain, which is very well-suited for reconstruction of the velocity gradients at nodes close to the domain boundaries. Indeed, if velocity gradients were to be calculated from neighbouring vectors located under the free surface (where the velocity is forced to zero), an artificial shear layer would be generated in the vorticity field over the free surface. Therefore, to avoid this effect, interpolations were conducted at each grid node in the aerial domain over spatial patches containing the $N = 16$ nearest velocity vectors located above the wave profile. The procedure was thus to subdivide the data into smaller aerial domains that were spline interpolated, and glued together at common edges by polynomials that could be computed using information in the neighbouring spline coefficients themselves. Size of patches (i.e. the number $N = 16$ of interpolated vectors) was determined from typical structure sizes in the air flow.

The instantaneous streamlines patterns $Z = f(X)$ were obtained following the method of Perry and Tan (1984). A predictor-corrector method was used to integrate $X(t)$ and $Z(t)$ in the following equations:

$$\frac{\partial X}{\partial t} = u = f_1(X, Z), \quad (8a)$$

$$\frac{\partial Z}{\partial t} = w = f_2(X, Z), \quad (8b)$$

where the functions $f_1(X, Z)$ and $f_2(X, Z)$ were obtained by locally interpolating the data with two-dimensional STS functions, as in the procedure for vorticity computation.

A complete error analysis was conducted to evaluate both velocity and vorticity measurement accuracy and can be found in Reul (1998). Briefly, bias on the particle displacement estimate is mainly induced by the lag between particles motion and fluid motion ($\leq 1\%$), the three-dimensionality of the flow ($\leq 5\%$), the velocity gradients ($\leq 6\%$) and inaccuracies in the numerical determination of both the cross-correlation functions and the peak positions. The latter effect is dependent on both the wind speed and the magnification factor: the smaller the particle image displacements, the greater the bias due to the peak-locking phenomenon associated with subpixel interpolation (Fincham and Spedding 1997). We obtained a relative error on the velocity that is smaller than 5% if the local velocity is greater than 2.2 m s^{-1} when imaging with field of view *S1*, and if the local velocity is greater than 5.5 m s^{-1} with *S2*. At 0.5 m s^{-1} , it respectively reaches about 15% and 25% for *S1* and *S2*. To assess the uncertainty in the vorticity measurements, we performed numerical simulation using an Oseen vortex with characteristic scales determined from typical structures extracted from the separated flows. Whatever the vortex centre location relative to the grid data, the relative vorticity error averaged over the central part of the vortex (area extending from the vortex centre to where the radial vorticity falls to 20% of the maximum vorticity value at the centre) was found to be less than 12% if the field of view was set to *S1*, and less than 25% if it was *S2*.

2.4 Static Pressure Measurements

Complementary information about the turbulence in the separated airflow was obtained by measuring the static pressure just over the crests of a few breakers. The differential technique developed by Giovanangeli (1988), which briefly consists in the coupled measurement of the total pressure and dynamic pressure head, was used to estimate the static pressure. A tube containing a helium flow kept at constant pressure at one end together with a constant heat X-wire anemometer were thus installed at a fixed position, 15 mm higher than the breaking wave crests. The static pressure time series were obtained from:

$$P_s(t) = P_{t_{\text{mes}}}(t) - \frac{1}{2} \rho_{\text{air}} C_{pt}(\alpha) |\vec{U}(t)|^2 - \frac{1}{2} \rho_{\text{air}} |\vec{U}(t)|^2 \quad (9)$$

where $P_{t_{\text{mes}}}$ is the instantaneous total pressure, ρ_{air} the density of air, $C_{pt}(\alpha)$ is a factor that takes into account the effects of the flow incidence at the probe α on the dynamic pressure measurement (Giovanangeli 1988), and $\vec{U}(t)$ is the instantaneous flow velocity at the measurement point.

3 Results

3.1 General Behaviour of Typical Separated Flow Over Short Breakers

Observations of the airflow structure during the propagation of an unsteady breaking wave under moderate wind forcing are first presented. The wind speed in the free-stream was set

to $U_o = 5.38 \text{ m s}^{-1}$ and wave groups were generated with an initial potential energy of $Epl_o = 0.0075$ and wave energy was focused at $x_b = 4.5 \text{ m}$. The duration between the end of the group generation and the time of passage of the breaking wave at position $x_b = 4.5 \text{ m}$ was measured and used to trigger the PIV acquisitions. Measurements were first conducted with the field of view S2 to visualize the flow over almost a complete breaker wavelength. Successive PIV measurements were acquired at a rate of 7.5 Hz during the propagation of the highest wave within a group. Figure 6a, b show the attached flow over part of the first wave that was propagating downwind of a breaker. A sudden change in the structure of the high-vorticity layer just above the interface occurred when the breaking wave trough began to cross the camera field of view (Fig. 6c, d). As seen a time step later (see Fig. 6e, f), the airflow was clearly separated over this unsteady breaking wave. The incident shear layer at the breaking crest thus departed from the interface at a point where the slope of the free surface exhibited an abrupt change. This separated shear layer developed downwind of the crest until it re-attached above a point somewhere at the interface downwind of the trough of the wave.

A well-defined recirculating motion is observed between that separated layer and the free surface. The flow exhibits the structure of a separation bubble. Downwind of the reattachment point (see Fig. 6c, d), a new sub-boundary layer developed in the vicinity of the water surface. A rising motion is observed above that layer, leading to the development of rotational structures in the free stream, well above the air–water interface. During the propagation of the breaker, the whole separated flow region was convected in the lee of the breaking crest.

Key parameters describing the flow structure can be defined and more detailed information can be extracted from higher resolution measurements, by decreasing the size of the CCD camera’s field of view. The flow fields captured over two wavelength-fractions of a typical spilling breaker using the field of view S1 and same wind wave conditions as previous example are shown in Fig. 7. The instantaneous *separating streamline* was defined as the locus of negative vorticity maxima in the separated shear layer. Streamline patterns were not used for this purpose because they are not Galilean invariant. Although it evolved slightly during propagation, the breaker wavelength λ was approximated from successive imaging of the water surface at 7.5 Hz. We defined positions along the profile using the wave phase relative to the crest θ . The separation and reattachment points: θ_S and θ_R , were respectively defined as the points along the profile where the vertical distance between the separating streamline and the interface was greater, and respectively smaller, than twice the PIV technique vertical resolution. The thickness of the separated-flow region downwind of the crest was parameterized by its mean height, defined as $h_s = A/\lambda$, where A is the area between the wave profile and the separation streamline. The along-wind extent of the separated-flow region was parameterized by the non-dimensional reattachment length, given by $L_R = (\theta_R - \theta_S)/2\pi$.

As seen in Fig. 7, the free shear layer that develops downwind of the separation point has an initial structure similar to a plane mixing-layer: it is sufficiently thin and high above the water surface not to be influenced by the latter. The separating streamline is therefore approximately horizontal in the first half of the separation bubble. As shown by Reul et al. (1999), small-scale vortices are shed in the initial region of the separated-layer downwind of the separation point and convected at approximately 40% of U_o . As it develops further downwind, this new shear layer is subjected to strong stabilizing curvature effects, to an adverse pressure gradient and substantial interactions with the water surface around the reattachment point. Due to the adverse pressure gradient, part of the fluid from the shear-layer is thus flowing backward to feed the recirculation region. The recirculation area is not a dead air zone since the maximum backflow velocity is approximately 20% of U_o and it exhibits a dynamically significant vortex. This structure is locally three-dimensional since the streamlines pattern

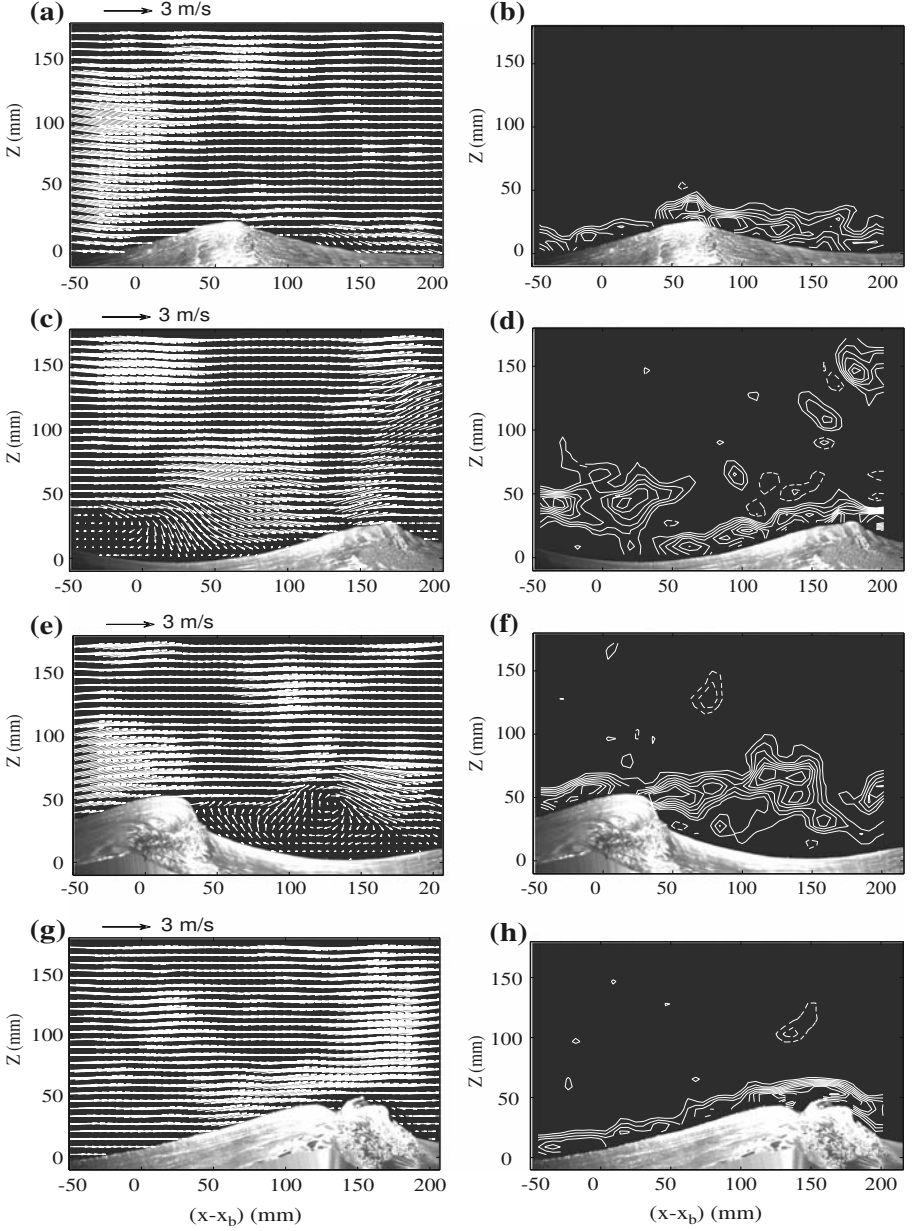


Fig. 6 Instantaneous velocity fields in the laboratory frame (left panels) and corresponding vorticity fields (right panels) in the airflow at four successive times over a breaking wave during its propagation. (**a, b**) acquisition at t_0 , (**c, d**) $t_0 + 135$ ms, (**e, f**) $t_0 + 270$ ms and (**g, h**) $t_0 + 405$ ms. In the right panels, solid lines and dashed lines respectively represent iso-level of negative and positive vorticity. The minimum vorticity and increment between each level are respectively $|\omega_n^{\min}| = 80 \text{ s}^{-1}$ and $\Delta\omega_n = 35 \text{ s}^{-1}$. The wind speed in the free stream is $U_o = 5.38 \text{ m s}^{-1}$

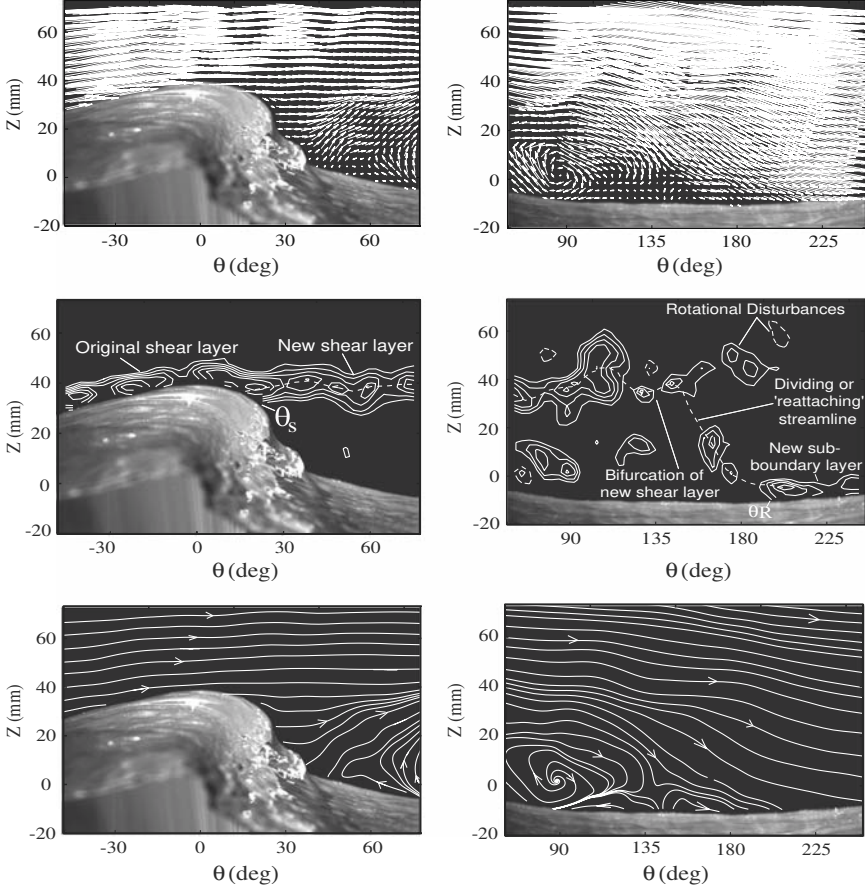


Fig. 7 Airflow instantaneous velocity distributions in the laboratory frame (Top panels), corresponding contours of constant positive (dashed lines) and negative (solid lines) vorticity (middle panels), and corresponding instantaneous streamline patterns (bottom panels), over sections of a transient spilling breaking wave. Left panels represent the flow over part of the breaker 135 ms after right panels. Minimum and incremental levels of vorticity are both $|\omega_n^{\min}| = \Delta\omega_n = 80 \text{ s}^{-1}$

show a spiral diverging from a focal point at its center: $\theta \simeq 90^\circ$ and $Z \simeq 0 \text{ mm}$ (Tobak and Peake 1982). Rotational structures are also generated in the separated-layer approximately where it bifurcates down towards the reattachment point. They form disturbances that spread above the new sub-boundary layer downwind of the separation bubble.

The general separated flow structure as just described above may be mainly affected by changes in the strength of the adverse pressure gradient and/or the characteristics of the incident shear boundary layer. Both factors are essentially controlled by the wave crest dynamics and the wind forcing intensity.

3.2 Qualitative Effects of Breaking Crest Unsteadiness

During a complete breaking event, the dynamic of the water flow in the region of the crest is highly unsteady. Before breaking, a wave is thus steepening until it reaches its maximum

steepness at incipient breaking. A patch of rough water then appears at the interface near the crest and the turbulent motions within that patch evolve strongly during the rest of the event. To determine the effects of such hydrodynamic intermittencies on the separation bubble structure, a second series of measurements were conducted. The wind speed in the free stream and the wave group's initial potential energy were kept the same as in the first set of measurements. The wave energy within the groups was however focused at the following successive positions: $x_b = 4.45, 4.55, 4.6$ and 4.7 m. The flow field was thus captured over very similar breaking waves but at different stages of the breaking process. We used the field of view *S2* in order to get at first a global picture of the effects of breaking unsteadiness on the separated airflow patterns.

As shown in Figs. 8 and 9, the separated airflow structure was strongly dependent on the stage of evolution of the breaking process. Prior to breaking (Figs. 8b, 9b), when the wave crest was approximately 1 wavelength upwind from the focusing point position, the high-vorticity layer was attached to the interface. When the crest reached about half the wavelength from the breaking point position (Figs. 8a, 9a), although no visible whitecap can be seen at the crest, a small separation bubble was generated: the shear layer departed from the interface at a point slightly downwind of the crest and re-attached around the wave trough. The flow within the separation bubble was a small vortex with very low vorticity. The flow was then captured over waves at a stage of incipient breaking and maximum steepness. In such cases (Figs. 8, 9c,d), the separated shear layer was lying higher over the water surface and re-attached farther downwind. At incipient breaking, the separation points appeared to lie closer to the crest than in the previous stages, at points where the wave profiles exhibited a sharp geometry. The blowing up of a low speed air mass with significant vorticity was often observed downwind of the reattachment point. When the flow fields were measured over fully breaking waves (Figs. 8, 9e–h), the general flow structure was conserved but the separation bubbles' vertical and horizontal extent were greater and the disturbances generated by the separated shear layers downwind of reattachment were intensified.

At the end of the breaking process, we noticed that the separation bubbles' extent slightly decreased.

3.3 Effects of Breaking Crest Geometry and Wind Forcing Intensity

The previous qualitative observations strongly suggest that kinematic and dynamic changes of the water flow at a crest during a breaking event are responsible for the concomitant evolution of the separated airflow structure. Although we had no way to quantify the kinematics of the flow at the water surface, the main geometrical characteristics of the crests could be extracted from the imaged wave profiles and linked with the estimated separation bubble geometry. For this purpose, the flow was captured over breaking waves with intensities ranging from micro-breaking, to spilling and violent plunging by progressively varying the wave packets initial potential energy from $Epl_o = 0.0021$ up to 0.0104 (see Table 1). The wave energy was kept focused at $x_b = 4.5$ m. Also, this set of measurements was first conducted at a fixed wind-speed $U_o = 5.38 \text{ m s}^{-1}$ to investigate the effects of various crests geometry on the airflow structure without changing the incident boundary-layer characteristics.

3.3.1 Incipient Air Flow Separation and Crest Geometry

In order to discuss the crest geometry influence on the early stages of the separation process, examples of the flow vorticity fields over two very similar micro-breakers ($Epl_o = 0.0021$

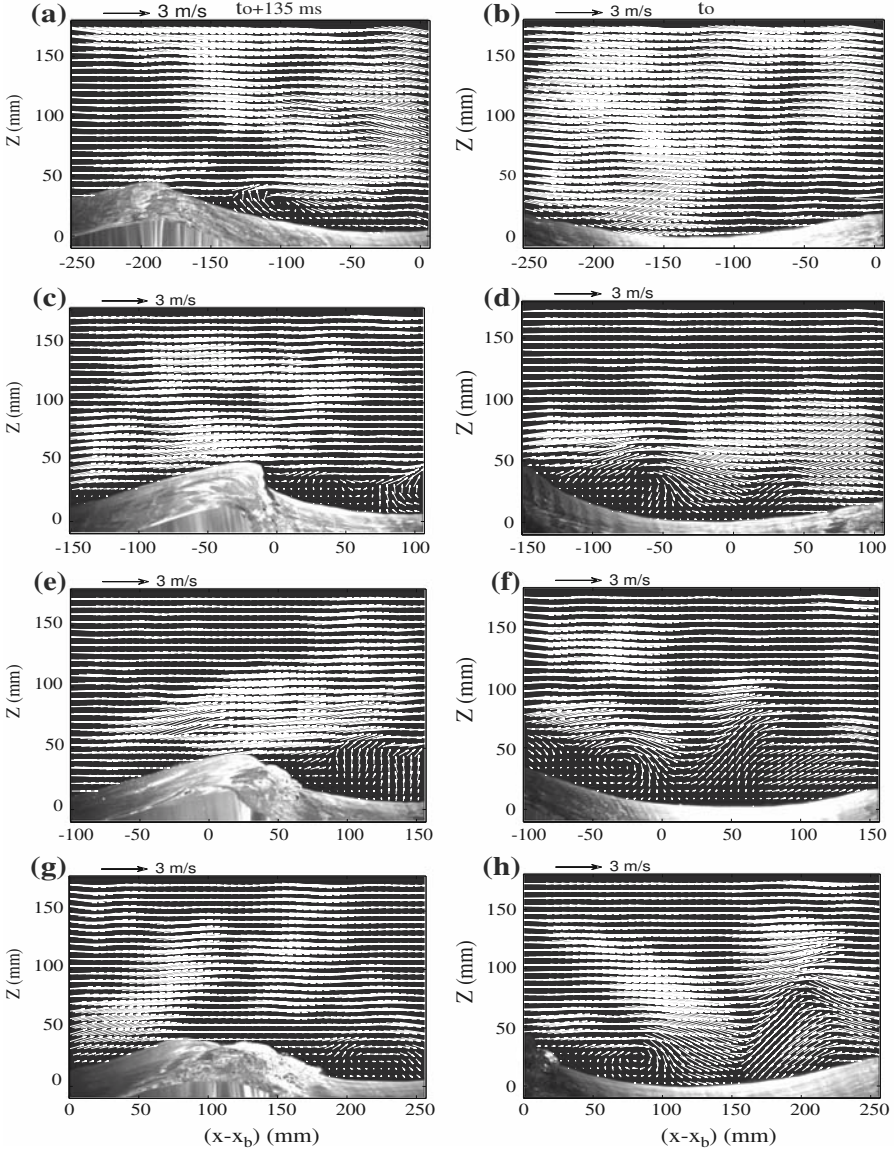


Fig. 8 Instantaneous velocity fields in the laboratory frame measured over four distinct waves at various stages of the breaking process. Each left panel represents the flow field over a wave measured 135 ms after the one seen in the right panel. **(a, b)** the wave is not breaking ($x_b = 4.70$ m), **(c, d)** the wave is at incipient breaking ($x_b = 4.6$ m), **(e, f)** the wave is fully breaking ($x_b = 4.55$ m), **(g, h)** the wave is at the end of the breaking process ($x_b = 4.45$ m)

in both cases with identical incident boundary layer at the crest) are first presented. As seen in Fig. 10, the airflow was separated above the upper wave, thereafter denoted wave A, but stayed attach over the lower wave, thereafter denoted wave B. Parameters describing the breaking waves geometry as defined by Bonmarin (1989), are given in Table 3; y_{\min} and y_{\max} are vertical distances between the mean water level and the wave trough and crest,

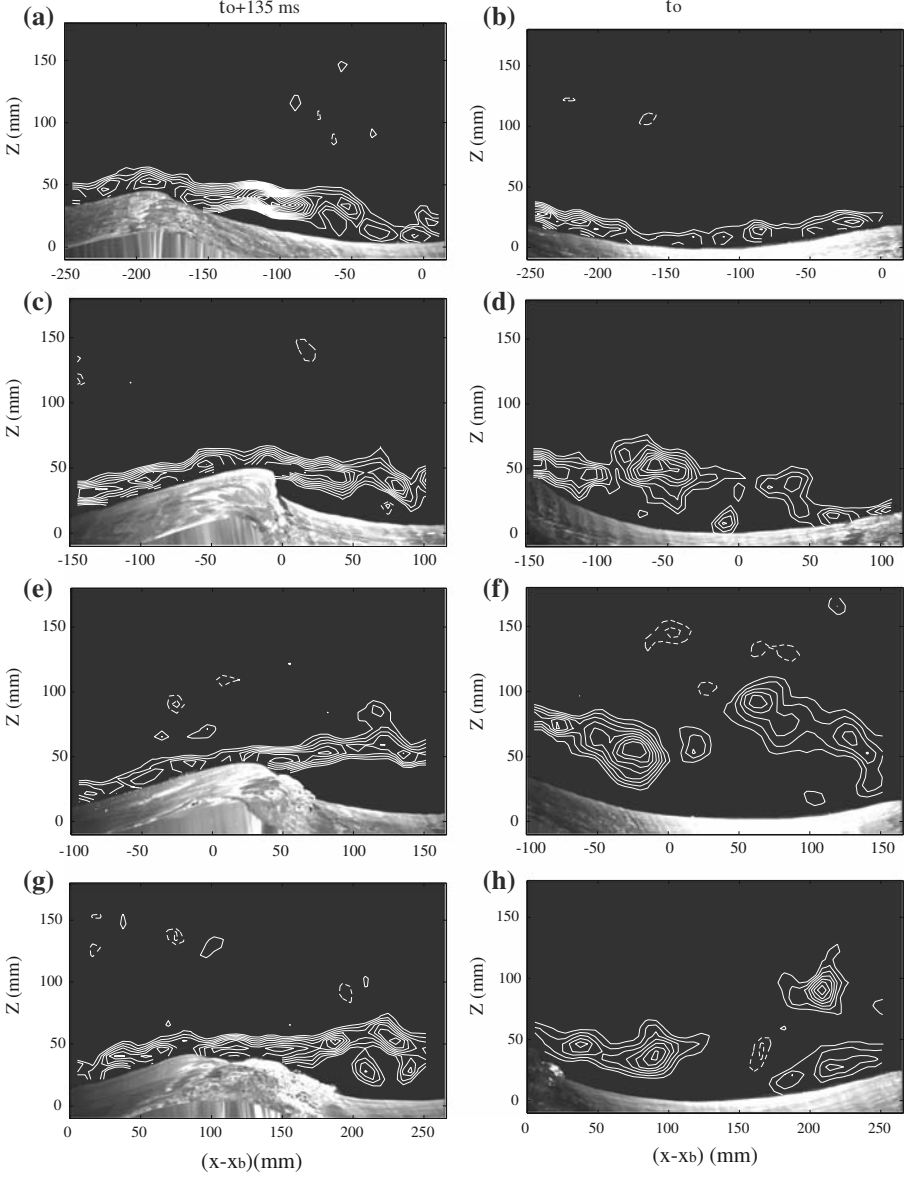


Fig. 9 Instantaneous vorticity fields corresponding to the images shown in Fig. 8. Minimum vorticity and increment are the same as those given in Fig. 6

respectively. $F1$ is the forward horizontal length from zero-upcross point of the wave profile to wave crest and $F2$ is the backward horizontal length from wave crest to zero-downcross point of the wave profile; $\varepsilon_{\text{crest}} = y_{\text{max}}/F1$ and $\delta_{\text{crest}} = y_{\text{max}}/F2$ are the crest front and back steepnesses, respectively; $\mu = y_{\text{max}}/(y_{\text{max}} + y_{\text{min}})$ and $\lambda_v = F2/F1$ are respectively the vertical and horizontal asymmetry factors. The Reynolds number based on the crest height: $Re_{y_{\text{max}}} = U_o y_{\text{max}}/\nu_{\text{air}}$ is also given, where ν_{air} is the air kinematic viscosity.

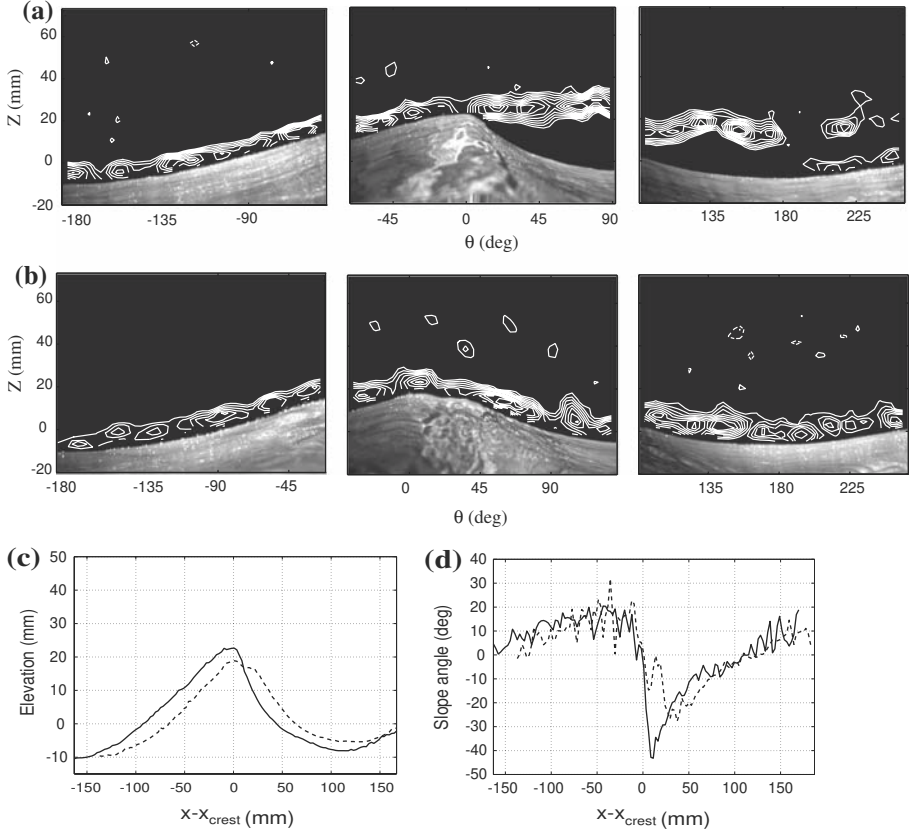


Fig. 10 Effects of the wave crest geometry on the airflow. **(a)** and **(b)**: contours of constant positive (dashed lines) and negative (solid lines) vorticity over two distinct waves during their propagation. Their is a 135 ms delay between each image from right to left. The wind speed in the free-stream was in both cases $U_o = 5.38 \text{ m s}^{-1}$, but the initial potential energy input into the group was $Epl_o = 0.0042$ for **(a)** and $Epl_o = 0.0021$ for **(b)**. Minimum and incremental levels of vorticity are both $|\omega_{\min}| = \Delta\omega = 150 \text{ s}^{-1}$. **(c)** wave profiles extracted from images in **(a)** (solid line) and **(b)** (dashed line); **(d)**: slope angle along the profiles (same conventions than in **(c)**)

Table 3 Parameters describing the geometry of waves A and B

Wave #	y_{\min} (mm)	y_{\max} (mm)	λ (mm)	$Re_{y_{\max}}$	F1 (mm)	F2 (mm)	$\varepsilon_{\text{crest}}$	δ_{crest}	μ	λ_v
A	8.0	22.6	278.2	10469	43.6	91	0.52	0.25	0.737	2.1
B	5.4	19.6	265	9060	68.5	63	0.28	0.31	0.78	0.92

As illustrated in Fig. 10c and Table 3, although both waves had very similar crest heights and wavelengths, the crest front-steepness $\varepsilon_{\text{crest}}$ and the horizontal asymmetry factors λ_v for wave B were approximately two times smaller than for wave A. Moreover, as illustrated in Fig. 10d, wave A profile over which the air flow is separated exhibits a much higher local slope maximum $\phi_{\max} = \max(\partial\eta/\partial x)$ downwind of the crest ($\phi_{\max}^A \simeq 43^\circ$) than wave B profile ($\phi_{\max}^B \simeq 27.8^\circ$).

These results suggest that the separation process can only be sustained at the early stages of breaking if the wave crest geometry is strongly asymmetric and exhibits high local slopes downwind of the crest. From an ensemble of PIV measurements over incipient breaking waves, we found that waves over which the flow is separated always exhibit $\phi_{\max}^{\text{crit}} \geq 35^\circ$. This is consistent with previous AFS observations over purely wind generated waves (Kawai 1981), for which a critical slope for AFS apparition was found to be of 0.6 ($\equiv \phi_{\max}^{\text{crit}} \geq 30^\circ$).

As shown in Dabiri and Gharib (1997), the upward vorticity flux of surface-parallel vorticity ω_y through a fluid free surface given in natural curvilinear orthogonal coordinates is

$$v_{\text{air}} \left(\frac{\partial \omega_y}{\partial r} \right)_{r=0} = \frac{\partial u_s}{\partial t} + \frac{1}{\rho_{\text{air}}} \frac{\partial P}{\partial s} + g \cos \theta + \frac{1}{2} \frac{\partial u_s^2}{\partial s} \quad (10)$$

where \mathbf{r} is the upward unit vector normal to the free surface, \mathbf{s} is the unit vector parallel to the free surface, and perpendicular to \mathbf{r} , and \mathbf{y} is the unit vector parallel to the free surface and perpendicular to \mathbf{s} and \mathbf{r} . In our 2D case, \mathbf{y} is normal to the PIV imaged plane. In Eq. 10, ω_y is the surface parallel vorticity, u_s is the interface velocity parallel to the 2D free surface, ρ_{air} is the air density, P is the pressure, θ is the angle of the surface with respect to the gravity vector, \mathbf{g} ($\theta = \pi/2 + \phi$). As theoretically shown by Banner and Melville (1976), AFS can occur over water waves only if a kinematic stagnation point exists at the air-sea interface. Assuming one follows a stagnation point in a frame moving at the wave crest speed, $u_s|_{r=0} = 0$ through the stagnation point lifetime, and Eq. 10 simplifies as :

$$v_{\text{air}} \left(\frac{\partial \omega_y}{\partial r} \right)_{r=0} = \frac{1}{\rho_{\text{air}}} \frac{\partial P}{\partial s} + g \sin \phi. \quad (11)$$

For the shear layer to be separated at such stagnation point, the upward vorticity flux in Eq. 11 must be positive. This is possible only if the pressure gradient along the interface is adverse (i.e., $\frac{\partial P}{\partial s} > 0$). Moreover, Eq. 11 shows that the greater the adverse pressure gradient and the profile slope ϕ , the greater the upward vorticity flux, and the more intense the separation process at stagnation points. The measurements over waves A and B illustrate that the adverse pressure gradient strength is mainly governed by the breaking wave crest front-steepness $\varepsilon_{\text{crest}}$ and the horizontal asymmetry factor λ_v .

3.3.2 Development of the Separated Zones

Once the air flow is separated over a breaking wave, the phenomenon can be either sustained, amplified or damped, the separated flow development depending on the wave crest geometry evolution during the breaking process. One can anticipate that if the crest front-steepness $\varepsilon_{\text{crest}}$ and the horizontal asymmetry factor λ_v increase, or decrease, during part of the breaking process, this shall induce concomitant growth, or decay, of the separated flow area.

To test these hypotheses, the instantaneous flow structure should be ideally measured at high frequency during the complete breaking process of a single wave. This was not possible with the PIV method we developed, which was limited to a rather low temporal rate of acquisition of 7.5 Hz. However, by varying the wave packets initial potential energy at a fixed wind-speed forcing of $U_o = 5.38 \text{ m s}^{-1}$, the flow structure could be captured over breaking waves with significantly varying crest geometry, simulating the potential stages of breaking. In Fig. 11, we show the instantaneous velocity fields over four typical breaking waves in a frame moving at the crest speed. The corresponding crest geometrical parameters $\varepsilon_{\text{crest}}$, $Re_{y_{\max}}$, λ_v and ϕ_{\max} are given for each case. Clearly, the separated zone area is a function of the instantaneous crest geometry. The higher and the steeper the crest, the more developed the separated flow in the lee of the crest.

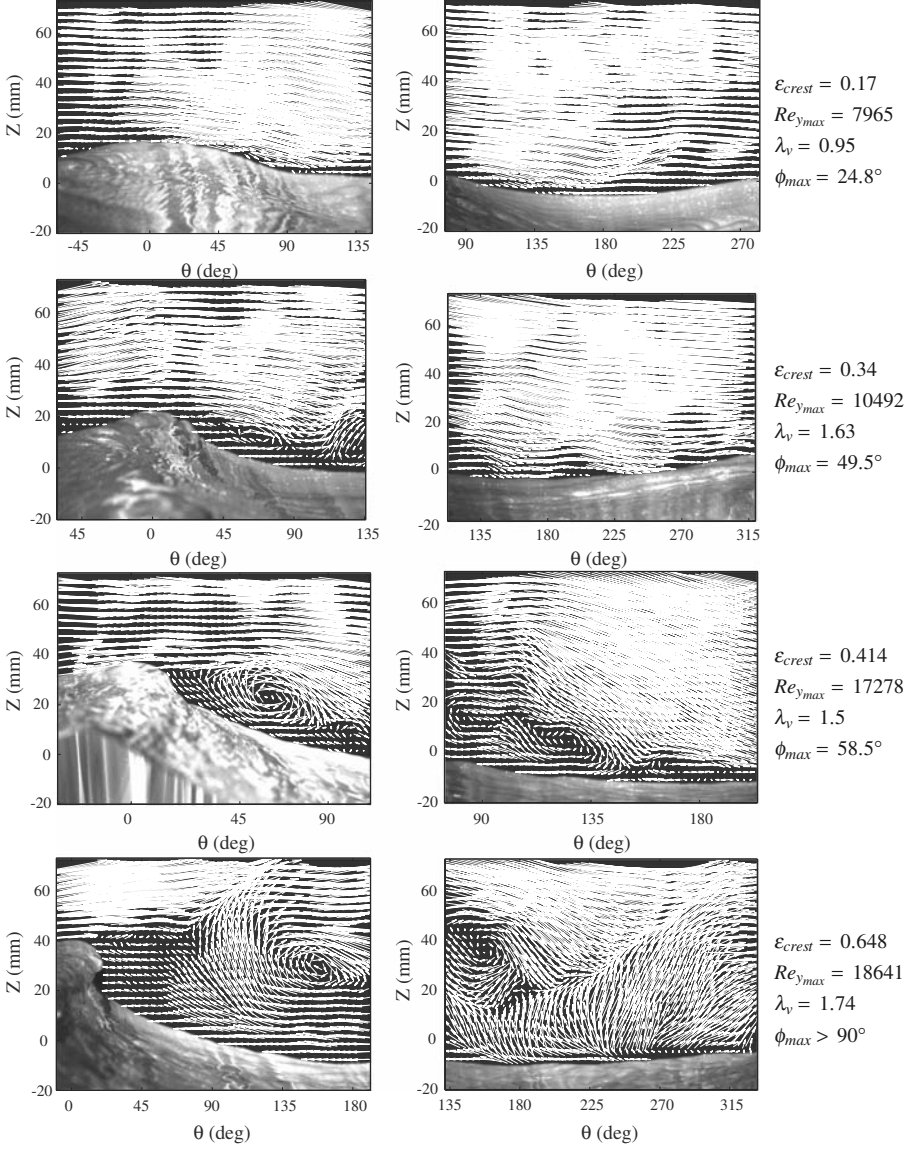


Fig. 11 Instantaneous velocity fields in the laboratory frame measured over four distinct waves breaking with various intensity. Their is 135 ms delay between each image from right to left. The wind speed in the free-stream was $U_o = 5.38 \text{ m s}^{-1}$. The potential energies input into the groups were $E_{plo} = 0.0021$ (micro-breaking) (a), 0.0055 (gentle-spilling) (b), 0.0075 (spilling) (c) and 0.0104 (plunging) (d)

To characterize the flow geometry we introduce the non-dimensional height of the separated layer h_s^* , defined by:

$$h_s^* = \frac{h_s}{\delta} \quad (12)$$

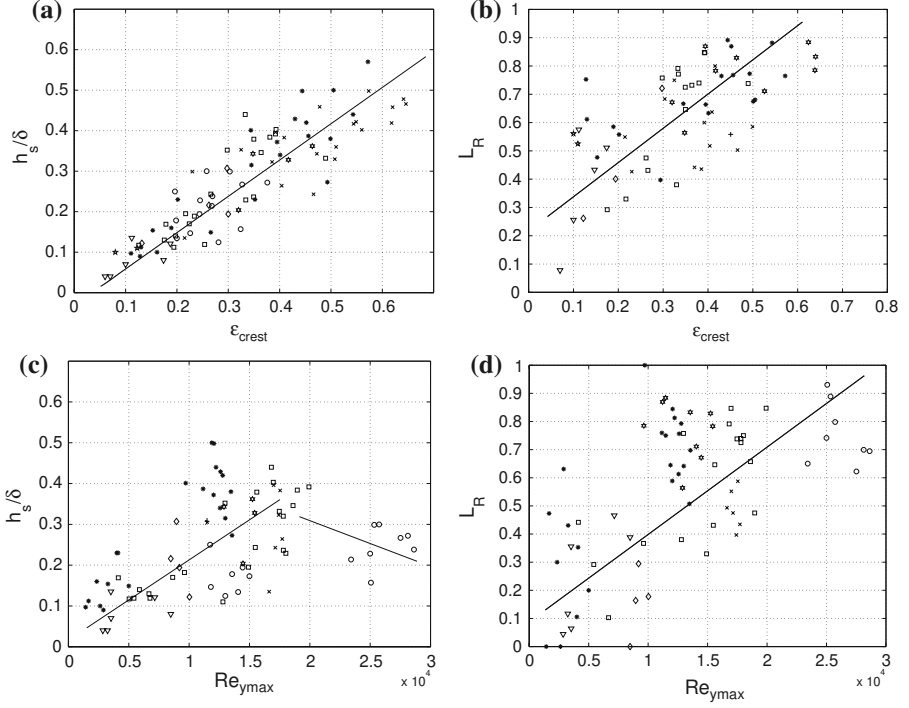


Fig. 12 Separation bubbles vertical (left panels) and longitudinal extent (right panels) as a function of (a, b) the wave crest-front steepness $\varepsilon_{\text{crest}}$, and (c, d) the Reynolds Number based on the crest height. \diamond : $U_o = 3.5 \text{ m s}^{-1}$ and $Epl_o = 0.0104$; $*$: $U_o = 5.38 \text{ m s}^{-1}$ and $Epl_o = 0.0104$; \square : $U_o = 7.9 \text{ m s}^{-1}$ and $Epl_o = 0.0104$; \circ : $U_o = 10 \text{ m s}^{-1}$ and $Epl_o = 0.0104$; ∇ : $U_o = 6.93 \text{ m s}^{-1}$ and $Epl_o = 0.0021$; $*$: $U_o = 6.93 \text{ m s}^{-1}$ and $Epl_o = 0.0075$; \times : $U_o = 6.93 \text{ m s}^{-1}$ and $Epl_o = 0.0104$

where δ is the incident boundary-layer thickness given in Table 2. Statistical analysis of the dependencies of the separated layer height h_s^* and reattachment length L_R as function of the crest geometry factors was then performed for a large range of breaking wave types, varying the wind-speed forcing and the initial potential energy in the coalescent wave packets.

Results are given in Fig. 12, which illustrates the measured dependencies of h_s^* and L_R with the crest front steepness $\varepsilon_{\text{crest}}$ and the Reynolds number based on the crest height $Re_{y_{\text{max}}}$. Whatever the incident wind forcing strength, Figs. 12 (a, b) show that there are net correlations between the separated flow vertical and horizontal extent with $\varepsilon_{\text{crest}}$.

Although the data dispersion is greater, the separated flow downwind and vertical extent are also observed to depend significantly with $Re_{y_{\text{max}}}$. While the height of the separated flow is measured to increase with $Re_{y_{\text{max}}}$ up to a critical Reynolds number of about 2×10^4 , after which it is decreasing, the reattachment length is found to be a continuously increasing function of $Re_{y_{\text{max}}}$. This is consistent with reported behaviour of separated flows past solid obstacles (Kim and Chung 1995).

3.4 Three-dimensionality of the flow

Because separated flows are associated with vortices and recirculation zones, determining airflow separation topologies over breaking waves may help formulating more realistic

models of the wind turbulence for air-sea interaction problems. The instantaneous streamline patterns corresponding to the flow fields shown in Fig. 11 are illustrated in Fig. 13. In the frame moving at the crest speed velocity, the centre of separation bubbles are critical points, i.e. points at which the magnitude of the velocity vector vanishes. In general, these points are foci towards which streamlines converge (attracting focus) or from which they diverge (repelling focus). As often reported in separated flow literature (e.g., Tobak and Peake 1982; Perry and Chong 1987), these singularities show that the flow in the separation bubble is locally three-dimensional. In general, we observed that the centre of the captured separation bubbles are repelling foci. However, in some cases like the example given in the second panel from top ($Re_{y_{\max}} = 10492$) in Fig. 13, we observed the opposite trend.

This suggests that we captured the flow in either growing or decaying stages of the unsteady separation process. During vertical extension of the separated layer (separation bubble growth), the flow is stretched vertically and incoming fluid is needed to continuously supplement the flow in the separation bubble. Contrarily, during decaying stages, the flow is compressed and fluid particles quit the separated bubbles laterally at their centre.

In cases with very intense separation (e.g., example at $\varepsilon_{\text{crest}} = 0.648$ and $Re_{y_{\max}} = 18641$ in Fig. 13), the recirculating motions are accompanied by intense vertical fluid “bursts” at reattachment. This is a universal feature of vortex-induced separation (Doligalski et al. 1994) associated with wall interactions. Highly rotational vortices interacting with a surface indeed induce strong adverse pressure gradients at the surface that generate three-dimensional turbulent motions. This phenomenon is illustrated in the lower right plot of Fig. 13 as diverging streamlines close to the interface.

3.5 Air Flow Separation Impact on the Wind Stress

For some PIV images, we evaluated the tangential shear stress at the closest distance $\varepsilon \simeq 1.2$ mm between valid PIV measurement points and the air/water interface:

$$\tau_{\text{tang}}(\varepsilon) = \mu_{\text{air}} \left(\frac{\partial u_s}{\partial r} \right)_{r=\varepsilon} \quad (13)$$

where u_s is the tangential airflow velocity along the wave profile. In the S_1 field-of-view configuration, ε was varying between about 1 and 1.5 mm. We evaluated $\tau_{\text{tang}}(\varepsilon)$ for both separated and non separated flows with a wind speed in the free-stream set to $U_o = 6.93 \text{ m s}^{-1}$ ($u_* = 0.347 \text{ m s}^{-1}$). As illustrated in Fig. 14a, the tangential shear stress above the wavy interface for a non separated flow is maximum over the wave crest and minimum above about the wave trough. The amplitude of the shear stress at the crest is almost twice the wavelength-averaged shear stress ($\langle \tau_{\text{tang}}(\varepsilon) \rangle_{\lambda} \simeq 0.0067 \text{ Pa}$). For a separated flow (see Fig. 14b), the shear stress amplitude exhibits a very large drop off in the separation bubble. For that example, the wavelength-averaged shear stress was indeed $\langle \tau_{\text{tang}}(\varepsilon) \rangle_{\lambda} \simeq 0.0021 \text{ Pa}$, but its average value in the separation bubble was $\langle \tau_{\text{tang}}(\varepsilon) \rangle_{X \in [X_S; X_R]} \simeq 0.0004 \text{ Pa}$, which is almost five times less. The tangential stress above the breaking wave profile does not exhibit spikes at reattachment but grows progressively downwind from zero at reattachment to a value at the next crest approximately that found at the upwind breaking crest. While indicative, we recall here that the reported measurements do not represent the actual surface stress, being measured at a height relatively well-above the viscous sublayer. Higher resolution PIV measurements would be required to obtain such information.

Measurements of the static pressure just over the crest of few breakers were conducted (at about 15 mm height above the crests) to give also an indication of the pressure across the imaged separated shear layers. As the pressure probe crossed the separated shear-layers, large

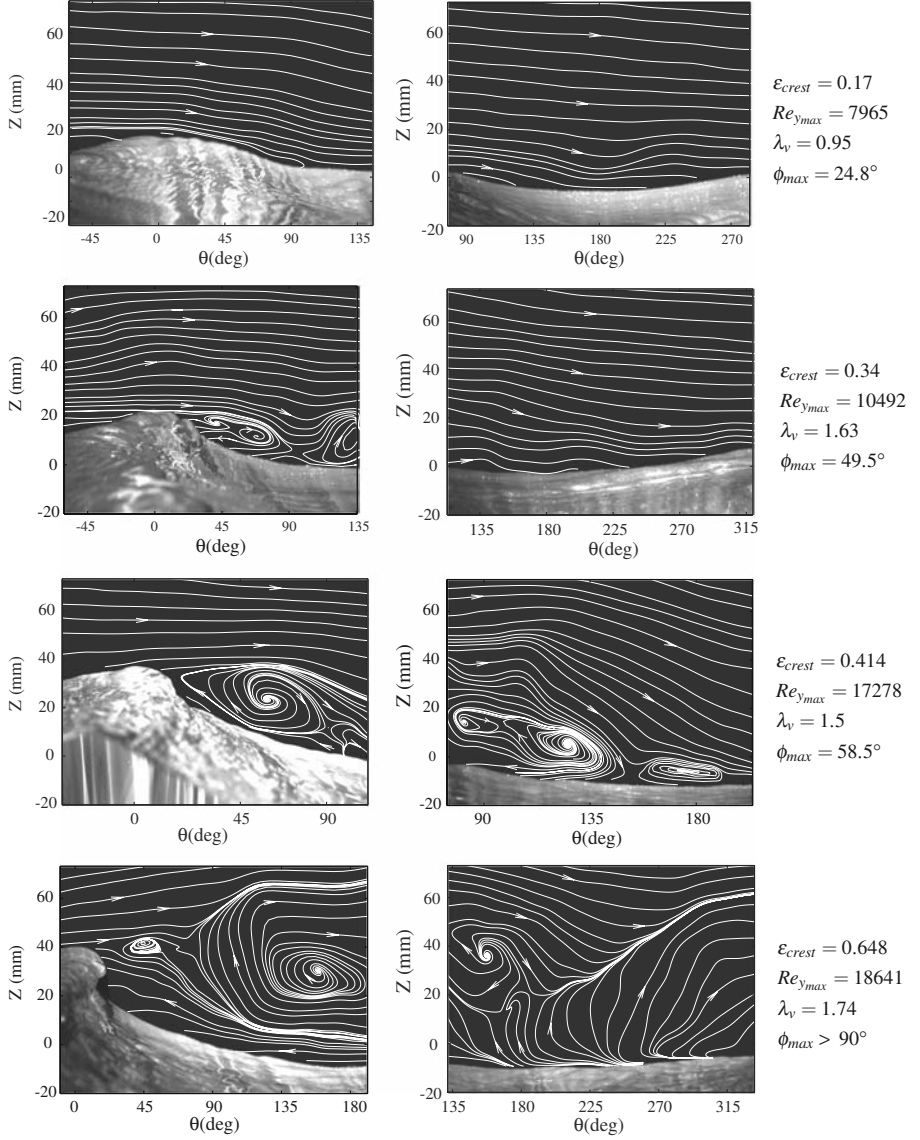


Fig. 13 Instantaneous streamline patterns corresponding to the flow fields shown in Fig. 11

pressure drops were measured. As illustrated in Fig. 15a, these pressure drops were observed to reach about four times the static pressure overall standard deviation σ_p . As discussed in Saathoff and Melbourne (1997), this is typical of separated layers past solid obstacles. The measurements presented here were unfortunately not useful in determining the static pressure exactly at the surface, which is the actual quantity required to evaluate the form drag at the interface. Nevertheless, the instantaneous pressure/slope correlation at the height of the pressure measurements is illustrated in Fig. 15b. At such levels above the interface,

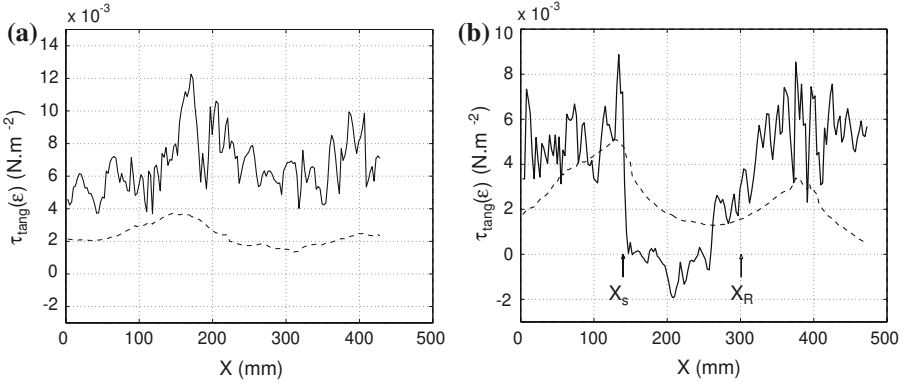


Fig. 14 Tangential stress distribution (solid curves) along the wave profiles (dashed curves) at a distance of approximately $\varepsilon \simeq 1.2$ mm from the air/water interface. (a) non separated airflow; (b) separated airflow

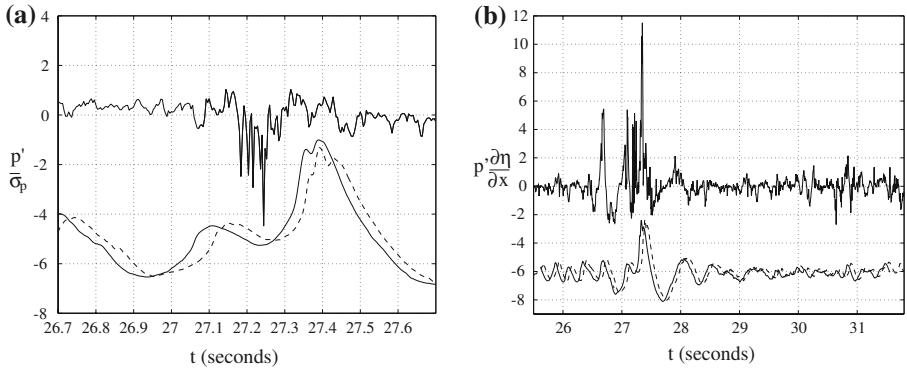


Fig. 15 (a) Typical static pressure drops measured within a separated layer over a breaker. Thick curve is p'/σ_p (b) Instantaneous product of static pressure p' by wave slope $\partial\eta/\partial x$ during the passage of a breaking wave at 15 mm above the crest level. Thick curve is $p'(\partial\eta/\partial x)$. In both figures, thin and dashed curves are surface elevation signals measured at $x = 4.45$ m and $x = 4.55$ m, respectively

it is clear that airflow separation induced by propagating breaking waves strongly affect the wind pressure/wave slope correlation.

4 Conclusion and Discussion

One of the most debated open questions of small-scale air sea interaction is concerned with the role of breaking waves. Understanding the airflow dynamics above short breaking waves is of key importance for the parametrization of the momentum, mass and heat transfer between atmosphere and ocean. However, despite intensive theoretical and experimental investigation conducted over the last five decades, the structure of the turbulent flow over breaking waves is still largely unknown. It is now established that local air-flow separation occurs along with wave breaking, enhancing the local wind stress. Although Kudryavtsev and Makin (2001) recently made a significant effort to develop a realistic theoretical model of the phenomena, key physical aspects of the processes involved are not yet fully accounted for (like sepa-

rated vortex turbulent interactions with the free surface at reattachment, impact of separated airflow intermittencies on the net momentum transfer from air to water during a complete breaking event). Therefore, it is still not clear if the wind input to breaking waves with air-flow separation is large enough to be important in the spectral balance of short ocean wind waves.

To advance in such study, we therefore used the DPIV to detail the formation and evolution of the air-flow velocity, vorticity and streamline patterns over the water surface during the passage of isolated breaking waves propagating in groups. The airflow was thus captured over single breaking waves, propagating in mechanically-generated wave groups and forced by the wind. By varying the wind speed and initial characteristics of the groups, the airflow structure was captured over waves at different stages of the breaking process, and breaking with various intensities. These unsteady breakers were about 0.3 m-wavelength short gravity waves, exhibiting relatively young wave age ($1 < c/u_* < 5$).

For various levels of breaking intensity and wind forcing conditions, the measurements show that the air flow separates systematically downwind of unsteady breaking crests and serves as a strong intermittent source of turbulence in the air. The instantaneous airflow separated from a sharp breaking crest is very similar to backward facing step process. Thus, for the moderate wind speed range studied (below 10 m s^{-1}), we consistently observed airflow separated structure with well defined recirculation bubbles advected in the lee of breaking crests. The separation bubbles are however strongly unsteady, with spatio-temporal time scales mainly driven by the dynamical evolution of the breaking crest during the overall breaking process. The dynamics and geometrical properties of the separation bubble (height of the separated layer, reattachment length) are shown to be highly correlated with the instantaneous geometry of the wave crest. The steeper the wave crest and the larger the Reynolds number based on the crest height, the higher the separated layer and the farther downwind the reattachment point. Our observations are therefore very consistent with the Jeffreys's theory (1925) hypothesis, in which the modelled energy flux to the surface through sheltering mechanism is correlated with surface wave slope statistics.

Blow up of low speed air mass was very often observed downwind of the separated airflow reattachment, as also previously reported in Kawai (1981) for separation over pure wind waves. Measured vorticity fields reveal that this apparent blow-up flow is indeed associated with rotational structures generated by vortex pairing in the separated shear layer, sufficiently far away from the crest. Our measurements suggest that these vortices are advected downstream of the reattachment point. For backward facing step with characteristic height scale h , the separated boundary layer relaxes to an equilibrium state approximately at a distance of about $80h$ from the step. By analogy, and assuming breaking waves steepness of about $ak \simeq 0.2$, the turbulent flow downstream of a standing breaking wave would be perturbed downwind of the separation bubbles over a distance of about 2 to 3 wavelengths from the breaker crest. For unsteady breaking and associated unsteady separation, this distance might be an upper limit. Although we did not systematically analyze breaking wave induced wakes at several wavelength downwind of breakers, the airflow separated disturbances that propagate downstream might be an important source of air turbulence in a wavefield subjected to breaking. This might be particularly important in the context of modelling transport mechanisms of spray being sheared off the crests of the waves.

Instantaneous flow topology in separated bubbles over breaking wave displays specific features of three-dimensional separation patterns. Depending on the growing or decaying stages of the separated bubbles, critical point analysis show that the flow is laterally injected in or rejected from the separation bubbles, respectively. Of course the actual airflow over open ocean water waves is three-dimensional, and three-dimensionally turbulent. However,

in general, three-dimensionality of the airflow was observed being very localized to the core of separated vortices. It can be argued that a spanwise-averaged two-dimensional representation of the airflow vorticity will still capture the essence of what happens in the airflow over breaking waves.

The tangential stress measured above the viscous sublayer has also been measured along the breaking wave profile. As found, it drops dramatically within the separation bubble and does not exhibit spikes at reattachment. It grows progressively downwind from zero at reattachment to a value at the next crest approximately matching the upwind breaking crest value. Static pressure measurements revealed that large pressure drops are generated by vortices in the separated layer, as found in separated flows over solids. Although indicative, our measurement technique did not allow evaluation of the actual tangential and form drags at the interface during a breaking event. Nevertheless, the physics of the interactions between separated-layer generated air pressure fluctuations and the breaking wave interfaces is certainly more complex than in Jeffreys's type of theory. As discussed in McIntyre (2003), water waves can be systematically amplified by two irreversible, ratchet-like mechanisms that depend on spatio-temporal inhomogeneities, such as wind gustiness, airflow separation unsteadiness and wave groupiness. Neither mechanism is accounted for in Jeffreys's models. The first mechanism is simply the drag from what might be called Rossby or vorticity lee waves in the airflow downstream of water-wave groups. The second is the intermittent vertical mixing of spanwise horizontal vorticity in the airflow (Rossby-wave breaking), a highly nonlinear, non-Fourier-superposable mechanism. Air flow separation over breaking waves further enhances such irreversible momentum transport from air to water.

Future investigations are thus necessary to observe and quantify the actual momentum transport over breaking waves during the expected growth and decay of the induced separation bubble. It is indeed crucial to further establish the important mean and variances of the wavelength-averaged momentum transport during a complete breaking event. Despite our work provide a first glimpse at the velocity and vorticity fields over unsteady breaking waves, much needs to be done to better understand this class of flows. Advanced techniques in DPIV are now available and would allow the flow to be captured at higher spatial and temporal resolutions than as presented here, in particular to reach the unresolved viscous sublayers above the interface. The technique we developed could be as well readily used to specifically analyze the separation process and its statistics over purely wind-generated waves.

Acknowledgements The authors would like to thank Bertrand Chapron and Victor Shrira for very useful comments and criticism of the work presented in this paper. The constructive comments from two anonymous referees led to an improved paper.

References

- Agui JC, Jimenez J (1987) On the performance of particle tracking. *J Fluid Mech* 185:447–468
- Banner ML (1990) The influence of wave breaking on the surface pressure distribution in wind-wave interactions. *J Fluid Mech* 211:463–495
- Banner ML, Melville WK (1976) On the separation of air flow over water waves. *J Fluid Mech* 77:825–842
- Banner ML, Peirson WL (1998) Tangential stress beneath wind-driven air-water interfaces. *J Fluid Mech* 364:115–145
- Barnett TP, Kenyon KE (1975) Recent Advances in the Study of Wind Waves. *Rep Prog Phys* 38:421–437
- Belcher SE (1998) Turbulent flow over hills and waves. *Ann Rev Fluid Mech* 30:507–538
- Bonmarin P (1989) Geometric properties of deep-water breaking waves. *J Fluid Mech* 209:405–433

- Chang P, Plate EJ, Hidy GM (1971) Turbulent air flow over the dominant component of wind-generated water waves. *J Fluid Mech* 47:183–208
- Coantic M, Favre A (1974) Activities in and preliminary results of, air-sea interactions research at I.M.S.T. *Adv Geophys* 16:391–405
- Dabiri D, Gharib M (1997) Experimental investigation of the vorticity generation within a spilling water wave. *J Fluid Mech* 330:113–139
- DeLeeuw G (1986) Vertical profiles of giant particles close above the sea surface. *Tellus* 38B:51–61
- DeLeeuw G (1987) Near surface particle size distributions profiles over the North Sea. *J Geophys Res* 92:14631–614635
- Doligalski TL, Smith CR, Walker JDA (1994) Vortex interactions with walls. *Ann Rev Fluid Mech* 26:573–616
- Donelan MA, Haus BK, Reul N, Plant WJ, Stiassnie M, Graber HC, Brown OB, Saltzman ES (2004) On the limiting aerodynamic roughness of the ocean in very strong winds. *Geophys Res Lett* 31:L18306. DOI: 10.1029/2004GL019460
- Drennan WM, Donelan MA (1996) Nonlinear coalescing wave groups. In: Donelan M, Hui W, Plant W (eds) *The air-sea interface* Miami, pp 127–132
- Durst F, Melling A, Whitelaw JH (1981) *Principles and practice of laser-doppler-anemometry*, 2nd edn. Academic Press, London, 437 pp
- Fincham AM, Spedding GR (1997) Low cost, high resolution DPIV for measurement of turbulent fluid flow. *Exp Fluids* 23:449–462
- Gent PR, Taylor PA (1977) A note on separation over short wind waves. *Boundary Layer Meteorol* 11:65–87
- Giovanangeli JP (1988) A new method for measuring static pressure fluctuations with application to wind-wave interaction. *Exp Fluids* 6:156–164
- Griffin OM, Peltzer RD, Wang HT, Schultz WW (1996) Kinematic and dynamic evolution of deep water breaking waves. *J Geophys Res* 101:16515–516531
- Jeffreys H (1925) On the formation of water waves by wind. *R Soc Lond Proc Ser A* 107:189–206
- Kawai S (1981) Visualisation of air flow separation over wind wave crest under moderate wind. *Boundary Layer Meteorol* 20:547–569
- Kawai S (1982) Structure of air flow separation over wind wave crest. *Boundary Layer Meteorol* 23:503–521
- Kawamura H, Toba Y (1988) Ordered motion in the turbulent boundary-layer over wind-waves. *J Fluid Mech* 197:105–138
- Keane RD, Adrian RJ (1992) Theory of cross-correlation analysis of PIV images. *Appl Sci Res* 49:223–241
- Kim BN, Chung MK (1995) Experimental study of roughness effects on the separated flow over a backward-facing step. *AIAA J* 33:159–161
- Koga M, Toba Y (1981) Droplet distributions and dispersion processes on breaking wind waves. *Appl Sci Rep Tohoku Univ Ser5 (Tohoku Geophys J)* 28:1–25
- Kudryatsev VN (2006) On the effect of sea drops on the atmospheric boundary layer. *J Geophys Res* 111:C07020. DOI: 10.1029/2005JC002970
- Kudryatsev VN, Makin VK (2001) The impact of air-flow separation on the drag of the sea surface. *Boundary-Layer Meteorol* 98:155–171
- Kudryatsev VN, Makin VK (2007) Aerodynamic roughness of the sea surface at high winds. *Boundary-Layer Meteorol* 125:289–303. DOI: 10.1007/s10546-007-9184-7
- Longuet-Higgins MS, Smith ND (1986) Measurements of breaking waves. Implications for wind-stress and wave generation. In: Phillips OM, Hasselmann K (eds) *Wave dynamics and radio probing of the sea surface*. Inter-Union Commission on Reader Meteorology, Horwood Publishing, pp 257–264
- Makin VK (1998) Air-sea exchange of heat in the presence of wind waves and spray. *J Geophys Res* 103:1137–1152. DOI: 10.1029/97JC02908
- McIntyre ME (2003) Wind-generated water waves: two overlooked mechanisms? In: Sajjadi SG, Hunt JCR (eds) *Wind over waves II: forecasting and fundamentals of applications*. Horwood Publishing, pp 105–118.
- Merzkirch W (1974) *Flow visualization*. Academic Press, New York, 266 pp
- Mestayer PG, Van-Eijk AMJ, Leeuw GD, Tranchant B (1996) Numerical simulation of the dynamics of sea sprays over the waves. *J Geophys Res* 101:20771–720797
- Perry AE, Chong MS (1987) A description of eddying motions and flow patterns using critical-point concepts. *Ann Rev Fluid Mech* 19:125–155
- Perry AE, Tan DKM (1984) Simple three-dimensional motions in coflowing jets and wakes. *J Fluid Mech* 141:197–231
- Pierson WJ, Donelan MA, Hui WH (1992) Linear and nonlinear propagation of water wave groups. *J Geophys Res* 97:5607–5621
- Reul N (1998) Etude expérimentale de la structure de l'écoulement d'air au-dessus de vagues courtes déferlantes. PhD thesis, Université de la Méditerranée Aix-Marseille II ESM2, Marseille France.

- Reul N, Branger H, Giovanangeli JP (1999) Air flow separation over unsteady breaking waves. *Phys Fluids* 11:1959–1961. DOI: 10.1063/1.870058
- Saathoff PJ, Melbourne WH (1997) Effects of free-stream turbulence on surface pressure fluctuations in a separation bubble. *J Fluid Mech* 337:1–24
- Simpson RL (1989) Turbulent boundary-layer separation. *Ann Rev Fluid Mech* 21:205–234
- Spedding GR, Rignot EJM (1993) Performance analysis and application of grid interpolation techniques for fluid flows. *Exp Fluids* 15:417–430
- Tobak M, Peake DJ (1982) Topology of three-dimensional separated flows. *Ann Rev Fluid Mech* 14:61–85
- Touboul J, Giovanangeli J, Kharif C, Pelinovsky E (2006) Freak waves under the action of wind: experiments and simulations. *Eur J Mech - B/Fluids* 25(5):662. DOI: 10.1016/j.euromechflu.2006.02.006
- Weissmann MA (1986) Observations and measurements of air flow over water waves .In: Phillips OM, Hasselmann K (eds) *Wave dynamics and radio probing of the sea surface*. chap 23, pp 335–352
- Willert CE, Gharib M (1991) Digital particle image velocimetry. *Exp Fluids* 10:181–193
- Wu J (1969) A criterium for determining air-flow separation from wind-waves. *Tellus* 21:707–713